4D registration of serial brain's MR images: a robust measure of changes applied to Alzheimer's disease

Marco Lorenzi[1 2], Nicholas Ayache[1], Giovanni Frisoni[2], and Xavier Pennec[1]

[1] Project Asclepios, INRIA Sophia Antipolis, France
[2] LENITEM, IRCCS San Giovanni di Dio, Fatebenefratelli, Italy

Abstract. The study of neurodegenerative pathologies like Alzheimer's disease led to an increasing interest in the evaluation of the morphological changes in the brain over time. The recent availability of public longitudinal datasets requires new approaches to consistently measure the changes through sequences of MR images of a specific subject. Nonrigid registration represents an instrument to measure atrophy as geometric differences between pairs of scans. Among these methods, the Symmetric Log-Demons algorithm is a computationally efficient registration algorithm which defines the transformations as diffeomorphisms. In this work we propose a robust framework for the intra-subject nonrigid registration of serial MR images to evaluate the brain changes in time. The temporal consistency is obtained by integration of the structural changes at each time point into a 4-dimensional warping algorithm, to describe the subject-specific temporal trajectory. Moreover, we will show how to derive measurements of brain changes consistently along the spatial dimension, from the voxel to the regional level. Results on synthetic and real data show that, under this approach, the resulting deformations define smoother trajectories for the evolution of the changes. The accuracy of the measurements is also improved by reducing the influence of intra-subject variability and the biases affecting the data. The present method could represent the basis for the development of a robust and consistent model of longitudinal changes at the population level.

1 Introduction

Alzheimer's disease (AD) is a neurodegenerative pathology of the brain, characterized by a co-occurrence of different phenomena, starting from the deposition of amyloid plaques and neurofibrillary tangles, to the development of functional loss and finally to cell deaths [12]. In particular, although the loss of cells is one of the final results of the pathological process taking place in the brain, it has been shown that the monitoring of structural changes provides a way to track the evolution of the disease, even at the incipient or pre-symptomatic stages [21]. Structural MR images represent a feasible and reproducible instrument for the study of the brain's integrity. The recent availability of public studies like

the "Alzheimer Disease Neuroimaging Initiative" (ADNI) [17] provides the research of data representing the complete history of the pathological process of Alzheimer's: from the healthy condition to mild cognitive impairment (MCI), and finally to the advanced stages of the disease.

In the recent past, computational anatomy acquired increasing weight in the analysis of medical data and several methods were developed to study the brain in the *cross-sectional* (evaluating differences between different subjects) and *longitudinal* (evaluating changes in time from serial data of the same subject acting as his own control) settings. While the cross-sectional approach highlights the main differences between clinical groups, the longitudinal perspective is more useful in detecting the subtle changes related to the biological processes. A consistent integration of the longitudinal approach into a group-wise analysis represents the final goal for the development of a comprehensive model of disease evolution.

Longitudinal Measures. From the longitudinal perspective, large efforts in neuroimaging were made to evaluate the changes occuring in the brain between pairs of scans. We can broadly define two main approaches for the detection of atrophy. The first one is represented by the global measurement of changes at the regional level by the detection of the volume changes as intensity differences of the scans [13], through the integration on regions of interest [11], or segmentation of specific areas [3].

The second is based on the detection of local geometrical differences by means of nonrigid registration. Examples of techniques based on nonrigid registration in longitudinal studies are voxel compression maps (VCM) [10], voxel/tensor-based morphometry (VBM,TBM) ([22],[6]), RAVENS maps [20] and cortical pattern matching (CPM) [26]. Local techniques provide global measures as well, by integration of the Jacobian Determinant of the deformation in the selected regions, and direct comparisons of local vs global measures have been provided [4].

While the above approaches are based on the assessment of image-to-image changes (a 3-D problem), the study of measurements on time-series was less explored, probably due to the historical difficulties in collecting large longitudinal dataset.

The 4-dimensional problem. The consistent evaluation of changes across serial images is a fundamental requirement to gain stability and robustness of the measurements, with higher accuracy in detecting biological phenomena like pathological trends. The registration of time series images plays a central role in many research fields, such as cardiac imaging [18] and motion analysis [19]. In the field of neuroimaging, a real 4D registration procedure for serial images was introduced in [23], where a subject-specific 4D template is warped to match the sequence of serial images. The study introduced the idea of Gaussian smoothing along a multidimensional neighborhood, to impose spatial and temporal constraints on the resulting 4-dimensional deformation field.

The new generations of registration algorithms are based on *diffeomorphisms*, invertible and differentiable mappings which guarantee higher accuracy, stability and smoothness properties. Recently, a study on frontotemporal dementia [2], introduced consistent longitudinal intra-subject registration with the "large

deformation diffeomorphic metric mapping"' (LDDMM) theory [16], by use of diffeomorphisms parametrized by time varying velocity fields. In the study, the diffeomorphisms matching the baseline image to the related serial images were sampled in a standardized time range to produce a subject-specific description of the temporal trajectory of the brain changes. Another remarkable use of the LDDMM framework for the analysis of longitudinal images was presented in [7] to perform a regression of the brain shapes as a function of age. Based on LDDMM, a complete framework for the consistent 4-dimensional registration of shapes was presented in [8]. While from a theoretical point of view LDDMM is the most consistent and theoretically founded framework for the study of diffeomorphisms, the high complexity and the computational requirements often prevent and limit the use in the practical contest, especially for the analysis on volumetric images in longitudinal datasets, due to the increasing number of registrations required.

The aim of the present work is to develop a computationally efficient algorithm for the diffeomorphic registration of serial MRI data to provide spatially consistent atrophy measurements, from the local to the regional level, within a temporally consistent framework.

2 Spatial and temporal consistency in the Demons

2.1 Non-Linear Registration: the algorithm.

The Symmetric Log-Demons algorithm looks for the diffeomorphic transformation ϕ which minimizes the intensity difference between a fixed image F and a moving image M [28]. The deformation ϕ belongs to the one-parameter subgroup of diffeomorphisms generated by a stationary velocity field $\mathbf{v}$ and is parametrized through the exponential operation, $\exp(\mathbf{v})$, defined by the following ODE:

$$\frac{\partial \phi(x,t)}{\partial t} = \mathbf{v}(\phi(x,t)), \tag{1}$$

with initial condition $\phi(x,0) = id$. The transformation is recovered at the parameter value $t = 1$, i.e. $\phi(x) = \phi(x,1)$. The use of stationary velocity fields simplifies the LDDMM problem and leads to an optimal compromise between approximation and efficiency for computationally tractable solutions. For example, the exponential operation is efficiently implemented in the Demon's algorithm by taking advantage of the "scaling and squaring" property of the one-parameter subgroups. This allows to compute the final parametrization as the iterative composition of successive exponentials [1]. The registration of the images F and M is achieved through the alternating minimization of the following energy

$$E(\mathbf{v},\mathbf{v_x}) = \underbrace{\frac{1}{\sigma_i^2}\|F - M\circ\exp(\mathbf{v_x})\|^2_{L_2} + \overbrace{\frac{1}{\sigma_x^2}\|\log(\exp(-\mathbf{v})\circ\exp(\mathbf{v_x}))\|^2_{L_2}}^{E_{\mathrm{reg}}(\mathbf{v},\mathbf{v_x})}}_{E_{\mathrm{corr}}(\mathbf{v},\mathbf{v_x})} + \frac{1}{\sigma_T^2}\mathrm{Reg}(\mathbf{v}), \tag{2}$$

The minimization scheme is alternatively operated with respect to the two variables $\mathbf{v}$ and $\mathbf{v_x}$ in two steps:

Minimization step. The energy $E_{\text{corr}}(\mathbf{v}, \mathbf{v_x})$ is first minimized to find an unregularized correspondence $\mathbf{v_x}$ to match the images F and M. The infinitesimal velocity $\partial\mathbf{v}$ for the minimization is computed in a closed form and the correspondence field $\mathbf{v_x}$ is updated consistently within the log-domain representation using the Baker-Campbell-Hausdorff (BCH) approximation for the composition of exponentials.

Regularisation step. Finally, the functional $E_{\text{reg}}(\mathbf{v}, \mathbf{v_x})$ is optimized with respect to $\mathbf{v}$. Following [15], we can obtain a closed form for the regularization step by convolution. As defined in [5], the regularization term $\text{Reg}(\mathbf{v})$ can be generally expressed in terms of an isotropic differential quadratic form (IDQF) $Q_k(\mathbf{v}) = \alpha_k \partial_{i_1 \dots i_k} \mathbf{v}_{i_{k+1}} \partial_{i_1 \dots i_k} \mathbf{v}_{i_{k+1}}$, where $\partial_{i_1 \dots i_k}$ is the derivative composition $\partial_{i_1} \dots \partial i_k$. We note that with the choice $\alpha_1 = 1$ and $\alpha_k = 0, \forall k \geq 2$, we retrieve the classical harmonic regularizer $\|\nabla \mathbf{v}\|^2$. The minimization will be then operated on the functional:

$$E_{\text{reg}}(\mathbf{v}) = \int_\Omega \frac{\|\mathbf{v} - \mathbf{v_x}\|^2}{\sigma_x^2}\, dx + \int_\Omega \sum_{k=1}^{\infty} \left(\frac{Q_k(\mathbf{v})}{\sigma_t^{2k}} \right) dx, \tag{3}$$

where Ω represents the domain of interest. The term $\log(\exp(-\mathbf{v}) \circ \exp(\mathbf{v_x}))$ was linearized using the zeroth order approximation of the BCH formula, and the weight σ_T is considered as a term of the regularizer to preserve the shape of the impulse response in case of high order regularization terms [5]. Differentiating now with respect to $\mathbf{v}$ yields the following condition:

$$\frac{\mathbf{v}(x) - \mathbf{v_x}(x)}{\sigma_x^2} + \sum_{k=1}^{\infty} \frac{(-1)^k}{\sigma_T^{2k}} \left(\alpha_k \Delta^k \mathbf{v}(x) \right) = 0,$$

and the resulting equation can then be minimized in the Fourier space to verify:

$$\hat{\mathbf{v}}(w) = \frac{1}{\left(\sum_{k=0}^{\infty} \frac{\sigma_x^2}{\sigma_T^{2k}} \alpha_k (w, w^T)^k \right)} \hat{\mathbf{v}}_{\mathbf{x}}(w), \tag{4}$$

Therefore, the optimal $\hat{\mathbf{v}}$ is obtained in the Fourier domain through the linear convolution of $\hat{\mathbf{v}}_{\mathbf{x}}$, thus leading to the Gaussian smoothing for the optimal solution $\mathbf{v} = G_\sigma * \mathbf{v_x}$, for an opportune σ.

2.2 Longitudinal registration via temporal regularization in the Demons

The longitudinal perspective in the registration process increases the dimensionality of the problem and adds a new level of estimation along the temporal dimension. Given serial images I_i, $i = 0 \dots n$, we propose to address the problem by borrowing the hierarchical approach from the statistical multilevel modeling:

- *First level of inference.* We estimate the deformations ϕ_i , $i = 1 \dots n$, and the relative velocity fields $\mathbf{v_i}$, to match each image I_i to the baseline I_0.

– *Second level of inference.* The $\mathbf{v_i}$ are used to estimate in the log-domain a subject-specific temporal trajectory $\bar{\mathbf{v}}_t$.
– *Hierarchical estimation.* The $\bar{\mathbf{v}}_t$ is then reintroduced in the first level as a prior term to drive the re-estimation of the deformations at each time point and the whole procedure can be iterated to improve the robustness. The prior $\bar{\mathbf{v}}_t$ introduces the information about the longitudinal progression.

The introduction of the new prior term $\bar{\mathbf{v}}_t$ in the Demons can be done at the regularization level (3), to constrain the solution for the optimal velocity $\mathbf{v}$:

$$E_{\text{reg}}(\mathbf{v}) = \int_{\Omega} \frac{\|\mathbf{v} - \mathbf{v_x}\|^2}{\sigma_x^2} + \frac{\|\mathbf{v} - \bar{\mathbf{v}}_t\|^2}{\sigma_t^2}\, dx + \int_{\Omega} \sum_{k=1}^{\infty} \left(\frac{Q_k(\mathbf{v})}{\sigma_t^{2k}} \right) dx, \qquad (5)$$

The optimization of the above formula lead to the same solution of the Demons regularization once we replace in (3) $\mathbf{v_x}$ by $\mathbf{v_M} = \frac{\sigma_t^2 \mathbf{v_x} + \sigma_x^2 \bar{\mathbf{v}}_t}{\sigma_t^2 + \sigma_x^2}$ and σ_x^2 by $\sigma_M^2 = \frac{\sigma_t^2 \sigma_x^2}{\sigma_t^2 + \sigma_x^2}$, to finally give

$$\mathbf{v} = G_\sigma * \left(\frac{\sigma_t^2 \mathbf{v_x} + \sigma_x^2 \bar{\mathbf{v}}_t}{\sigma_t^2 + \sigma_x^2} \right), \qquad (6)$$

The optimal velocity $\mathbf{v}$ for the Demons is then computed from the weighted average between the field given by the matching criteria $\mathbf{v_x}$ and the temporal prior $\bar{\mathbf{v}}_t$. The parameters σ_x and σ_t determine the trade-off between the spatial and temporal information, i.e. the belief that will drive the estimation of the deformation. Under this approach, the deformation will be estimated taking into account the global temporal evolution while still remaining consistent in the registration framework.
It has been previously proposed to perform longitudinal registration through regularization of the 4D deformation field in a 4-dimensional neighborhood, i.e. by minimization of the temporal gradient [23]. This approach represents a special case of the framework we introduced, where the prior $\bar{\mathbf{v}}_t$ is estimated through kernel regression from the sequence of the $\mathbf{v_i}$.

2.3 The Demons to consistently measure brain changes from the voxel to the regional level

The quantification of the amount of warping applied at each voxel by the dense deformation field is usually derived from the Jacobian matrix $\mathbf{J}$ of the deformation in terms of determinant, log-determinant, trace or the strain tensor $\mathbf{J}\mathbf{J}^T$. A global index of change can be extracted from the local information by:

– Integration of the Jacobian Determinant in the region of interest. This is an average measure of *volume change*.
– Evaluation of the flux of the deformation field across the surface enclosing the region, i.e. the amount of vectors flowing through the surface during the registration procedure. This is a value representing the *shift of the boundaries* of the surface required to match the homologous points during the registration process.

If the flux on a specific surface area is known, and so the average "force" applied on the infinitesimal surface element, we can derive a volume change index by comparing the volume enclosed by the shifted surface relative to the original surface. However, the direct computation of the flux represents a challenge and is usually highly sensitive to the localization of the boundaries. While this limitation prevented the use of the flux in favour of the more robust Jacobian determinant integration, surrogate intensity-based measures have been proposed ([11], [24]).

We will now follow the procedure derived from [9] and recently introduced in the Demons in [15], to show how to derive from the Log-Demons formulation a consistent way to integrate the local measure in the global indices of changes. From the formula (1), the instantaneous variation of the Jacobian determinant of the deformation can be expressed as:

$$\frac{\partial \det(\nabla\phi(x,t))}{\partial t} = \det(\nabla\phi(x,t))\,\mathrm{tr}\left(\nabla\phi(x,t)^{-1}\frac{\partial(\nabla\phi(x,t)}{\partial t}\right),$$

Reversing time and spatial derivatives in the trace and applying the chain rule we get:

$$\frac{\partial \det(\nabla\phi(x,t))}{\partial t} = \det(\nabla\phi(x,t))\,(\nabla.\mathbf{v}(x)\circ\phi(x,t)),$$

Given that $\phi(x,0) = \mathrm{id}$, we have $\log(\det(\nabla\phi(x,0))) = 0$, and we obtain the solution $\log(\det(\nabla\phi(x,t))) = \int_0^t \nabla.\mathbf{v}|_{\phi(x,h)}\,dh$. In particular,

$$\log(\det(\nabla\phi(x,1))) = \int_0^1 \nabla.\mathbf{v}|_{\phi(x,h)}\,dh, \tag{7}$$

The above formula states that, under the Demons framework, the log-determinant of the Jacobian of $\phi(x) = \phi(x,1)$ equals the integration of the divergence of the velocity field along the path described by the exponential.
Supposing now that Ω is a volume immersed in the vector field $\phi(x)$, we can integrate (7) to obtain:

$$\iiint_\Omega \log(\det(\nabla\phi(x,1)))d\Omega = \int_0^1 \left(\iiint_\Omega \nabla.\mathbf{v}|_{\phi(x,h)}\,d\Omega\right)dh, \tag{8}$$

We remember now the Divergence Theorem, which states that for a volume Ω immersed in a vector field $\mathbf{v}$ the following relationship holds:

$$\iiint_\Omega (\nabla.\mathbf{v})\,d\Omega = \oint_{\partial\Omega} \mathbf{v}\cdot\boldsymbol{n}\,d\partial\Omega,$$

where the second part of the equality represents the flux of the vector fields through the surface $\partial\Omega$.
Applying the Divergence Theorem to (8) finally gives:

$$\iiint_\Omega \log(\det(\nabla\phi(x,1)))d\Omega = \int_0^1 \mathrm{flux}_{\partial\Omega}(\mathbf{v}|_{\phi(x,h)})\,dh \tag{9}$$

The integration over the volume of interest of the log-determinant of the Jacobian of the deformation is equivalent to compute along the exponential path the flux of the velocity field across the corresponding surface.

Practical Consequences. First, the above formula provides a way to consistently compute the flow of the vector field during all the evolution followed along the parametrization, and not focusing only on the final transformation $\phi(x, 1)$. Second, we compute a shift between surfaces (right side of (9)) by integration on a volume (left side of (9)). This relieves the segmentation errors (and relative erroneous boundary detection) and allows to deal with uncertainties in the measures by integration on probabilistic masks, weighting the integral by the probability of the voxels to belong to the volume. Last, under this formulation we can clearly distinguish the difference between the integration of the Jacobian (volume change) and the integration of the log Jacobian (shift of the boundaries).

In the next sections we will use the index of *flux-derived volume change*, where the field across the surface given by the flux is approximated with a radial field on a sphere S_1 enclosing the same volume. We obtain a volume change index by comparing the volume of the resulting shifted sphere S_2 relatively to S_1.

3 Experiments and Results

3.1 A synthetic experiment

A synthetic example was simulated in order to mimic the typical problem of atrophy detection in Alzheimer's disease. The subject-specific temporal evolution reflects the underlying pathological process common to the whole population, with a certain variability due to the subjective progression and the biases affecting the data. We should be able to retrieve the subject-specific evolution, as well as the true pathological progression, attenuating the effects of noise and intra-subject variability.

We built a population of 30 "simplified brains", composed of noisy images of a sphere of grey matter surrounding a smaller sphere divided into separated white matter and CSF areas. The inter-subject variability was simulated by sampling the external and internal radius $(r_{\text{ext}0}, r_{\text{int}0})$ from normal populations with mean of respectively 33 and 7 voxels and variance of 1.

Longitudinal atrophy was then simulated by reducing the GM layer from both inward and outward in 4 time steps. Here, the subject-specific temporal variability was introduced by sampling at each time point t from radius $(r_{\text{ext}}(t), r_{\text{int}}(t))$ with:

$$\begin{aligned} r_{\text{ext}}(t) &= r_{\text{ext}0} - 3t + u_e \\ r_{\text{int}}(t) &= r_{\text{int}0} + 3t + u_i \qquad t = 1 \dots 4 \end{aligned} \tag{10}$$

with $u_e, u_i \sim N(0, 1)$. The Demons algorithm was used to warp each baseline image to the four follow-up images, and the flux-derived volume change was evaluated on the GM layer mask at each time point. For each sphere i, the four serial estimated velocity fields were used to estimate at each voxel x

the "subject-specific" temporal evolution $\bar{\mathbf{v}}_t^i(x,t)$ by fitting a linear model in time. The estimated temporal evolution $\bar{\mathbf{v}}^i$ was then used to constrain the new evaluation of the deformations using the previous formulation (6). We set the trade-off between spatial and temporal regularization $\frac{\sigma_t}{\sigma_x}$ at 0.5, 1 and 2 for experimental purposes. These values represent respectively double weight to the temporal information $\bar{\mathbf{v}}_t^i$, equal weight between spatial and temporal information, and double weight to the spatial information $\mathbf{v}_x$. The differences between the regularized and non-regularized flux-derived volume changes were assessed by correlation with the subject-specific, i.e. noisy, true volume change and the population-specific true underlying volume change given by the law (10).

Results. As shown in Fig. 1, the regularization procedure didn't significantly alter the magnitude of the estimated flux-derived volume changes. Table 1 shows the correlation between flux-derived volume changes and the true volume changes with the different regularizations. As expected, the temporal regularisation increased the correlation with the population volume change and attenuated the correlation with the noisy subject-specific trends. Finally, we tested an alternate optimization scheme iterating the estimation of the $\bar{\mathbf{v}}_t^i$ and the following deformations for 3 steps. This evaluation was carried out under the different ratio $\frac{\sigma_t}{\sigma_x}$ of 0.5, 1 and 2 and the results were not significantly different from those obtained with a single step approach (paired t-test).

Table 1: Correlation between flux-derived and manual derived GM layer percentage volume changes at different regularization values. The increase of the temporal regularization lead to increased correlations with the true underlying volume change.

$\frac{\sigma_t}{\sigma_x}$	none	2	1	0.5
Population volume change	0.916	0.940	0.942	0.944
Noisy volume change	0.9947	0.976	0.969	0.962

3.2 Experiment on Real Data

Longitudinal MRI scans taken within a 3 years period from 8 MCI subjects converted to Alzhiemer's dementia were selected from the ADNI dataset. The images were affine registered to the Talairach space (MNI152 template) and bias correction was performed using the N3 algorithm [27]. For each subject, the follow-up images were robustly aligned to the baseline and the intensities were equalized using a robust intensity correction algorithm [25]. The resulting follow up images were then non linearly registered to the baseline using the Demons algorithm with the following parameters: diffusion like sigma=1.5, fluid like sigma=0.5 and maximum update step length of 1 voxel. Finally, the flux-derived whole brain volume change was computed in the baseline probabilistic brain mask. The results were compared to the percentage brain volume change from manual tracings and to the automated measures obtained with the KN-BSI algorithm [14], all available from the ADNI database. The effect of the temporal regularisation was tested. As in the synthetic experiment, the sequence of velocity fields previously computed for each subject were used to estimate at each voxel x the subject-specific temporal evolution $\bar{\mathbf{v}}_t^i(x,t)$ through a linear

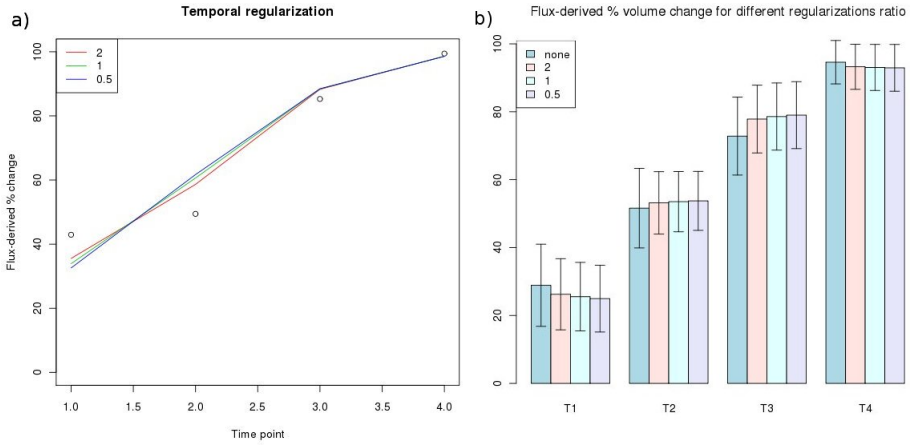

Fig. 1: Synthetic experiment. a) Subject-specific flux-derived volume change at the 4 time points without temporal regularization (black circles) and with different trade-off $\frac{\sigma_t}{\sigma_x}$ for the temporal constraint (coloured lines). Higher weights to the temporal constraint (from red to blue) lead to a more linear (regular in time) estimation of the progression. b) Mean and standard deviation of the flux-derived volume changes for the 30 brain spheres at the 4 different time points without temporal regularization and with different trade-off $\frac{\sigma_t}{\sigma_x}$ for the temporal constraint. At each time point, the regularization procedure slightly reduced the variance but didn't significantly change the magnitude of the estimation.

model with time as an independent variable. The fitted $\bar{\mathbf{v}}_t^i(x,t)$ were then used to constrain the new estimation of the deformations as in (6), testing different regularization weights for the trade-off between spatial ad temporal informations: $\frac{\sigma_t}{\sigma_x} = 0.5, 1, 2, 3, 4$.

Results. Figure 2 shows the relationship between flux-derived and manual derived whole brain volume changes. The correlation coefficient was 0.899 while on the same dataset the KNBSI algorithm scored 0.846. The correlation between flux-derived measures and KNBSI was 0.759, and the correlation between manual-derived volume changes and the mean Jacobian of the deformation in the brain mask was 0.825. Figure 3 illustrates the effects of the temporal regularization on the measurements of the flux-derived volume change and Table 2 summarises the correlation results between flux-derived and manual-derived volume changes under the different scenario. The temporal regularisation increases the correlation with the manual measures, and we can notice a bell shaped behaviour with the maximum value achieved using a spatio-temporal trade-off $\frac{\sigma_t}{\sigma_x} = 2$, i.e. putting half weight to the temporal information with respect to the spatial one.

Table 2: Correlation between flux-derived and manual derived percentage whole brain volume changes at different regularization values. The highest correlation is reached with a spatio-temporal trade-off $\frac{\sigma_t}{\sigma_x} = 2$.

$\frac{\sigma_t}{\sigma_x}$	none	0.5	1	2	3	4
Pearson's r	0.899	0.918	0.921	0.922	0.920	0.918

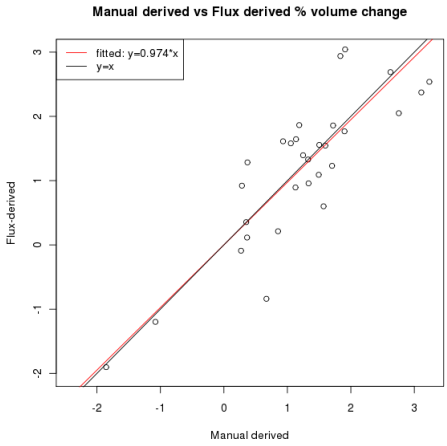

Fig. 2: Relationship between flux-derived and manual derived whole brain percentage volume changes.

4 Conclusion and further works

We proposed a complete framework to evaluate the longitudinal morphological changes in the brain via the consistent diffeomorphic registration of serial MR images. The experimental results exhibited accurate estimations accompanied by an increased regularity along the temporal dimension. The robustness is achieved through the introduction of a temporal prior to drive the estimation in the longitudinal setting and the definition of the flux-derived volume change, a measure consistently derived from the algorithm formulation. In the present study the prior was estimated using a linear model in time. Even though a linear progression could not track faithfully the real underlying biological process, this first order approximation led to reliable results in the 4-dimensional registration procedure. Moreover, the sample size from typical longitudinal clinical studies prevents the use of more elaborated models. Experimental results from weighted regression estimation, not showed in the present study, led to similar results to those obtained with classical linear regression, but at the expense of new parameters to calibrate. Further investigations will also be required in the definition of an optimal value for the spatio-temporal trade-off. The experiments on real data showed an interesting bell shaped behaviour for the trade-off value, with the maximum correlation with manual measurements obtained with a ratio between spatial and temporal weights of 2:1. This means that the linear model is not sufficient to describe the evolution of the deformations, but it introduces consistency and helps to improve the registration. We believe that the proposed approach could represent a robust instrument for tracking the brain changes and we are currently planning a large scale validation of the algorithm for the use in the clinical context. The present study introduces a hierarchical approach in the problem of the estimation of longitudinal trajectories, where the different levels are determined by the dimensionality of the problem. The structure naturally evolves into the highest levels of modeling where the different subject-specific

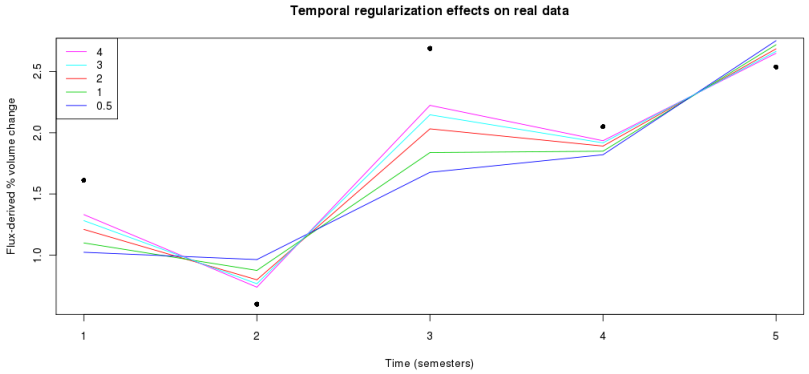

Fig. 3: Flux-derived brain volume change in time for a specific subject without temporal regularisation (black dots) and with different trade-off $\frac{\sigma_t}{\sigma_x}$ for the temporal constrain (coloured lines). As in the synthetic example, the weight on the temporal constraint led to a more linear (regular in time) estimation of the progression

trajectories will be used to develop a model for the population evolution. This point will require to merge the different subject-specific geometries consistently in a common reference space, and so the development of a precise and reliable method to transport the subject-specific longitudinal trajectories. Several strategies based on the Demons are currently under study.

References

1. Arsigny, V., Commowick, O., Pennec, X., Ayache, N.: A log-euclidean framework for statistics on diffeomorphisms. MICCAI 4190, 924 (2006)
2. Avants, B., Anderson, C., Grossman, M., Gee, J.: Spatiotemporal normalization for longitudinal analysis of gray matter atrophy in frontotemporal dementia. MICCAI pp. 303–310 (2007)
3. Barnes, J., Foster, J., Bojes, R., Pepple, T., Moore, E., Schott, J., Schaill, R., Fox, N.: A comparison of methods for the automated calculation of volumes and atrophy rates in hippocampus. NeuroImage pp. 960–963 (2010)
4. Boyes, Rueckert, Aljabar, et al.: Cerebral atrophy measurements using jacobian integration: Comparison with the boundary shift integral. NeuroImage 32 (2006)
5. Cachier, P., Ayache, N.: Isotropic energies, filters and splines for vectorial regularization. J. of Math. Imaging and Vision 20, 251–265 (2004)
6. Chetelat, G., Landeau, B., Eustache, F., Mezenge, F., Viader, F., de la Sayette, V., Desgranges, B., Baron, J.C.: Using voxel-based morphometry to map the structural changes associated with rapid conversion to mci. NeuroImage 27, 934–946 (2005)
7. Davis, B., Fletcher, P., Bullit, E., Joshi, S.: Population shape regression from random design data. ICCV 4, 375–405 (2007)
8. Durrleman, S., Pennec, X., Trouvé, A., Gerig, G., Ayache, N.: Spatiotemporal atlas estimation for developmental delay detection in longitudinal datasets. MICCAI 5761 (2009)
9. Evans: Partial differential equations. Graduate Studies in Mathematics 19 (1998)
10. Fox, N., Crum, W., Schaill, R., Stevens, J., Janssen, J., Rossnor, M.: Imaging of onset and progression of alzheimer's disease with voxel compression mapping of serial magnetic resonance images. Lancet 358, 201–205 (2001)

11. FreeBorough, P., Fox, N.: The boundary shift integral: An accurate and robust measure of cerebral volume changes from registered repeat mri. IEEE Transaction on Medical Imaging 16(5) (1997)
12. Jack, C., Knopman, D., Jagust, W., Shaw, L., Aisen, P., Weiner, M., Petersen, R., Trojanowski, J.: Hypothetical model of dynamic biomarkers of the alzheimer's pathological cascade. Lancet Neurol 9, 119–128 (2010)
13. Lemieux, L., Wieshmann, U., Moran, N., Fish, D., Shorvon, S.: The detection and significance of subtle changes in mixed-signal brain lesions by serial mri matching and spatial normaliation. Medical Image Analysis 2, 838–843 (1998)
14. Leung, K.K., Clarkson, M.J., Bartlett, J.W., Clegg, S., Jack, C.R., Weiner, M.W., Fox, N.C., Ourselin, S.: Robust atrophy rate measurement in alzheimer's disease using multi-site serial mri: 2 tissue-specific intensity normalization and parameter selection. NeuroImage 59 (2009)
15. Mansi, T., Pennec, X., Sermesant, M., Delingette, H., Ayache, N.: Logdemons revisited: Consistent regularisation and incompressibility constraint for soft tissue tracking in medical images. MICCAI (2010)
16. Miller, M., Trouvé, A., Younes, L.: On the metrics and euler-lagrange equations of computational anatomy. Annu. Rev. Biomed. Rev. 4, 375–405 (2002)
17. Mueller, S., Weiner, M., Thal, L., Petersen, R., Jack, C., abd J.Q. Trojanowski, W.J., Toga, A., Beckett, L.: The alzheimer's disease neuroimaging initiative. Neuroimaging Clin. 15, 869–877 (2005)
18. Peyrat, J., Delingette, H., Sermesant, M., Pennec, X.: Registration of 4d time-series of cardiac images with multichannel diffeomorphic demons. MICCAI 5242, 972–979 (2008)
19. Ren, W., Singh, S., Singh, M., Zhu, Y.: State-of-the-art on spatio-temporal information-based video retrieval. Pattern Recognition 42, 267–282 (2009)
20. Resnik, S., Goldszal, A., C., Davatzikos, Golski, S., Kraut, M., Metter, E., Bryan, R., Zonderman, A.: One year age changes in mri brain volumes in older adults. Cerebral Cortex 10, 464–472 (2000)
21. Ridha, B., Barnes, J., Bartlett, J., Godbolt, A., Pepple, T., Rossor, M., Fox, N.: Tracking atrophy progression in familial alzheimer's disease: a serial mri study. Lancet Neurol 5, 828–834 (2006)
22. Scahill, R., Schott, J., Stevens, J., Rossor, M., Fox, N.: Mapping the evolution of regional atrophy in alzheimer's disease: unbiased analysis of fluid-registered serial mri. Proc Natl Acad Sci 99, 4703–4707 (2002)
23. Shen, D., Davatzikos, C.: Measuring temporal morphological changes robustly in brain mr via 4-dimensional template warping. NeuroImage 21, 1508–1517 (2004)
24. Smith, S., Zhang, Y., Jenkinson, M., Chen, J., Matthews, P., Federico, A., Stefano, N.D.: Accurate, robust, and automated longitudinal and cross-sectional brain change analysis. NeuroImage 17 (2002)
25. Souplet, J.: Évaluation de l'atrophie et de la charge lésionnelle sur des séquences irm de patients atteints de sclérose en plaques. Thèse de sciences (PhD Thesis) (2009)
26. Thompson, P., Ayashi, K., Zubicaray, G., Janke, A., Rose, S., Semple, J., Herman, D., Hong, M., Dittmer, S., Dodrell, D., Toga, A.: Dynamics of gray matter loss in alzheimer's disease. The Journal of Neuroscience 23, 994–1005 (2003)
27. Tustison, N., Avants, B., Cook, P., Zheng, Y., Egan, A., Yushkevich, P., Gee, J.: N4itk: Improved n3 bias correction. IEEE Transaction in Medical Imaging 19 (2010)
28. Vercauteren, T., Pennec, X., Perchant, A., Ayache, N.: Symmetric log-domain diffeomorphic registration: A demons-based approach. MICCAI 5241, 754–761 (2008)